

PAPER • OPEN ACCESS

Static and dynamic transport properties of multi-terminal, multi-junction microSQUIDs realized with Nb/HfTi/Nb Josephson junctions

To cite this article: S Wolter *et al* 2022 *Supercond. Sci. Technol.* **35** 085006

View the [article online](#) for updates and enhancements.

You may also like

- [The 2022 applied physics by pioneering women: a roadmap](#)
Begoña Abad, Kirstin Alberi, Katherine E Ayers et al.
- [SQUIDs in biomagnetism: a roadmap towards improved healthcare](#)
Rainer Körber, Jan-Hendrik Storm, Hugh Seton et al.
- [Multi-terminal multi-junction dc SQUID for nanoscale magnetometry](#)
Alexander Y Meltzer, Aviram Uri and Eli Zeldov

Static and dynamic transport properties of multi-terminal, multi-junction microSQUIDs realized with Nb/HfTi/Nb Josephson junctions

S Wolter^{1,*} , J Linek² , T Weimann¹ , D Koelle² , R Kleiner²  and O Kieler¹ 

¹ Physikalisch-Technische Bundesanstalt, Bundesallee 100, D-38116 Braunschweig, Germany

² Physikalisches Institut, Center for Quantum Science (CQ) and LISA⁺, Universität Tübingen, Auf der Morgenstelle 14, D-72076 Tübingen, Germany

E-mail: silke.wolter@ptb.de

Received 6 April 2022, revised 7 June 2022

Accepted for publication 13 June 2022

Published 5 July 2022



CrossMark

Abstract

The progressive miniaturization of superconducting quantum interference devices (SQUIDs) used, e.g. for magnetic imaging on the nanoscale or for the detection of the magnetic states of individual magnetic nanoparticles causes increasing problems in realizing a proper flux-bias scheme for reading out the device. To overcome the problem, a multi-terminal, multi-junction layout has been proposed and realized recently for the SQUID-on-tip configuration, which uses constriction-type Josephson junctions (JJ). This geometry is also interesting for SQUIDs based on overdamped superconductor—normal metal—superconductor (SNS) JJ. We fabricated four-terminal, four-junction SQUIDs based on a trilayer Nb/HfTi/Nb process and study their static and dynamic transport properties in close comparison with numerical simulations based on the resistively and capacitively shunted junction model. Simulations and measurements are in very good agreement. However, there are large differences to the transport properties of conventional two-junction SQUIDs, including unusual phase-locked and chaotic dynamic states which we describe in detail. We further extract the current-phase relation of our SNS junctions, which turns out to be purely sinusoidal within the experimental error bars.

Keywords: low-temperature superconductors, nanotechnology, multi-terminal, multi-junction SQUID, niobium technology, current-phase relation, SNS Josephson junctions

(Some figures may appear in colour only in the online journal)

1. Introduction

Miniaturized superconducting quantum interference devices (SQUIDs) offer high spatial resolution and high sensitivity

* Author to whom any correspondence should be addressed.



Original content from this work may be used under the terms of the [Creative Commons Attribution 4.0 licence](https://creativecommons.org/licenses/by/4.0/). Any further distribution of this work must maintain attribution to the author(s) and the title of the work, journal citation and DOI.

for the detection and investigation of magnetic sources on the nanoscale. To achieve high spin sensitivities, even below $1 \mu_B/\text{Hz}^{1/2}$ (μ_B is the Bohr magneton) [1], and to improve their coupling, e.g. to individual magnetic nanoparticles (MNPs), nanowires or nanotubes [2–10], it is crucial to downscale the linewidth of the SQUID loop [11–13] and the size of the Josephson junctions (JJs) intersecting the loop. Therefore, direct current (dc) SQUIDs with lateral size in the μm range (microSQUIDs) or even sub- μm range (nanoSQUIDs) have received increasing attention during the last years [14, 15] and already have promising

applications for high-resolution scanning SQUID microscopy [1, 16–25]. Additionally, downscaling the dimension of the SQUIDs makes them insensitive to strong external magnetic fields [26, 27].

On the other hand, downscaling makes it increasingly difficult to modulate the magnetic flux through the SQUID using flux-modulation lines. An elegant solution has been presented in [28, 29], where the traditional two-junction SQUID-on-tip (SOT) [1] was replaced by a multi-terminal SOT configuration containing three or four junctions in the SQUID loop. Biasing the individual junctions allows adjusting the SQUID to optimal sensitivity for all values of an applied magnetic field. The SOT contains constriction-type JJs where self-heating leads to current voltage characteristics (IVCs) which are hysteretic under current bias and thus require a voltage bias to operate the device slightly above its critical current. Consequently, the analysis in [28] focused on the static behaviour and the critical current of the multi-terminal SOT.

The use of SNS-type JJs, where N indicates the normal conducting barrier of the junction and S denotes the superconducting electrodes, can allow for non-hysteretic IVCs of the individual junctions and consequently for a more traditional readout where the SQUID is current-biased in the resistive state. However, having in mind highly miniaturized SQUIDs, the problem of an adequate flux modulation remains and, thus, the concept of the multi-junction SQUID is also very attractive for SQUIDs based on SNS junctions. In contrast to asymmetric two-junction SQUIDs, where the asymmetry of the junctions or the SQUID loop and therefore the shift of the quantum interference pattern is chosen with the design, the multi-junction SQUIDs offer the possibility to shift the pattern continuously. Thus, the optimal working point can be adjusted precisely and independently of the parameter spread during the fabrication. Furthermore, the multi-terminal, multi-junction SQUIDs are superior to two-junction SQUIDs with direct injection feedback current to adjust the flux bias, since they offer two additional control currents, enhancing the electric tunability of the SQUIDs. This makes them more suitable for noise reduction schemes, which are based on periodic flux-bias switching of the SQUIDs [28, 30].

The dynamics of a conventional two-junction SQUID is understood very well on the basis of the resistively and capacitively shunted junction (RCSJ) model [31, 32]. Such an approach is also very reasonable for a multi-junction SQUID. However, one may expect nontrivial interactions of the four junctions and consequently a behaviour which may strongly deviate from a traditional device. This expectation motivates our theoretical and experimental study of the dynamics of SNS-type multi-junction SQUIDs, using a configuration with four junctions embedded in the SQUID loop. Connecting to [28] we first analyze the critical current of the device as a function of various control parameters. We then turn to the resistive state and study IVCs and voltage vs. flux modulation patterns, with the finding of several unusual dynamic states.

The organization of the paper and the main results are as follows. In section 2 we first introduce the mathematical model and subsequently use it to analyze the dynamics of a

4-JJ SQUID with (nearly) symmetric junctions. In the resistive state we find a complex interplay between phase-locked and chaotic states, leading, e.g. to an unusual hysteresis in the SQUID IVC and to multiple-valued voltage vs. flux modulation patterns. Section 3 focuses on the experimental device and contains a comparison of its transport characteristics to simulations. The section starts with some details on the fabrication and the design of the device (section 3.1) and then turns to a basic characterization in terms of critical current vs. flux patterns, IVCs and voltage vs. flux modulation patterns (section 3.2). The comparison between experiment and simulation shows that one of the junctions of the experimental device is in essence shorted (i.e. the junction has a very high critical current) so that effectively we have an asymmetric 3-JJ SQUID. Taking the actual device parameters into account we find excellent agreement between measurement and simulation. Section 3.3 focuses in more detail on the behaviour our device when one of the junctions is biased by an additional current. Here, a peculiar state is detected, where the junctions in one of the SQUID arms are in the resistive state, but with opposite dc voltages, while the junctions in the other arm of the SQUID remain in the zero-voltage state. Section 3.4 is devoted to the determination of the current-phase relation (CPR) of two of the JJs. The CPR's are extracted from the data by using a procedure introduced in [28] and turn out to be purely sinusoidal within the experimental error bars. Section 4 concludes our work.

2. Numerical simulations

2.1. Mathematical model

We consider the 4JJSQ as schematically depicted in figure 1, with four ports ($p = 1, \dots, 4$). Three independent currents I_1, I_2 and I_4 can be injected via ports 1, 2 and 4, respectively. The current I_3 to port 3 is used as a drain, i.e. we have $I_3 = I_1 + I_2 + I_4$. Each loop segment between neighboring ports contains one JJ; i.e. the SQUID loop is intersected by four JJs ($k = 1, \dots, 4$). We consider I_1 as a bias current and I_2 and I_4 as control currents, and we will discuss how the critical current I_{c1} (from port 1 to 3) and the voltage V_{SQ} (between port 1 and 3) will change with the control currents and with Φ_{ext} .

The Josephson current through the k th junction is $I_{J,k} = I_0 a_k \sin(\delta_k)$, with asymmetry parameters a_k and gauge-invariant phase differences δ_k of the superconducting wave functions across the k th JJ. Here, we define I_0 as the average $(I_{0,left-min} + I_{0,right-min})/2$ of the (noise-free) critical currents of those two JJs which have the lower critical current in the left and right SQUID arm, respectively. Accordingly, the sum of the asymmetry parameters of those two 'weakest JJs per SQUID arm' is 2. This choice for the definition of I_0 ensures that the (noise-free) critical current I_{c1} vs. Φ_{ext} for $I_2 = I_4 = 0$ of the 4JJSQ has a maximum $I_{c1,max} = 2I_0$.

Normalizing currents to I_0 , we obtain in normalized form for the Josephson currents $i_{J,k} = a_k \sin(\delta_k)$. To capture also dynamic properties of the 4JJSQs, we describe each

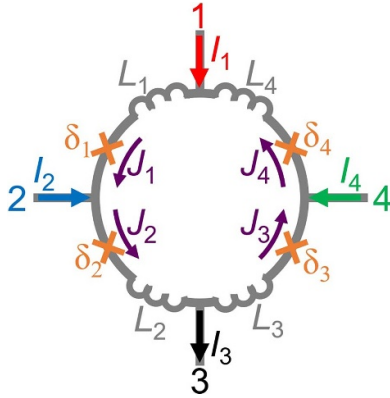


Figure 1. Schematic layout of the 4-terminal SQUID (with ports $p = 1-4$) intersected by 4 Josephson junctions ($k = 1-4$) with phase differences δ_k . The bias current I_1 , the drain current I_3 and the control currents I_2 and I_4 as well as the currents J_k through the k th junction are indicated by arrows. The inductances of the loop segments between the four ports are denoted by L_k .

junction within the resistively and capacitively shunted junction (RCSJ) model [31–33], i.e. we also consider quasiparticle currents through the junction resistance R , and displacement currents across the junction capacitance C . For simplicity, we assume that R and C are the same for all four JJs. The SQUID loop shall have a total inductance $L = \sum_{k=1}^4 L_k$, where L_k denote the inductances of the loop segments between the four ports (see figure 1).

In normalized form the RCSJ equations read:

$$\beta_C \partial_t^2 \delta_k + \partial_t \delta_k + a_k \sin(\delta_k) + i_{N,k} = j_k, \quad \text{for } k = 1, 2, \quad (1a)$$

$$\beta_C \partial_t^2 \delta_k + \partial_t \delta_k + a_k \sin(\delta_k) + i_{N,k} = -j_k, \quad \text{for } k = 3, 4. \quad (1b)$$

Here, $\beta_C = 2\pi I_0 R^2 C / \Phi_0$ is the Stewart-McCumber parameter with the magnetic flux quantum $\Phi_0 = h/2e \approx 2.0678 \cdot 10^{-15}$ Vs. In equation (1) time is normalized to $\Phi_0 / (2\pi I_0 R)$ and currents are normalized to I_0 . ∂_t indicates derivatives with respect to the normalized time. The currents $i_{N,k}$ denote normalized noise currents with (normalized) spectral density 4Γ , where $\Gamma = 2\pi k_B T / (I_0 \Phi_0)$ is the noise parameter.

The normalized currents j_k can be found from the conditions $i_1 = j_1 - j_4$, $i_2 = j_2 - j_1$, $i_3 = i_1 + i_2 + i_4 = j_2 - j_3$ and $i_4 = j_4 - j_3$. With the definition of an average circulating current $j_{\text{SQUID}} = \sum_{k=1}^4 j_k / 4$ one obtains:

$$j_1 = j_{\text{SQUID}} + i_1/2 - i_2/4 + i_4/4, \quad (2a)$$

$$j_2 = j_{\text{SQUID}} + i_1/2 + 3i_2/4 + i_4/4, \quad (2b)$$

$$j_3 = j_{\text{SQUID}} - i_1/2 - i_2/4 - 3i_4/4, \quad (2c)$$

$$j_4 = j_{\text{SQUID}} - i_1/2 - i_2/4 + i_4/4. \quad (2d)$$

Using (in dimensioned units) $\sum_{k=1}^4 L_k J_k + \Phi_{\text{ext}} = (\Phi_0 / 2\pi) [\delta_3 + \delta_4 - \delta_1 - \delta_2]$, the current j_{SQUID} can be related to the phase differences δ_k via:

$$j_{\text{SQUID}} = [-\delta_1 - \delta_2 + \delta_3 + \delta_4 - 2\pi(\varphi_{\text{ext}} + \varphi_b)] / (\pi \beta_L), \quad (3)$$

with the screening parameter $\beta_L = 2I_0 L / \Phi_0$. Here, φ_{ext} is the magnetic flux (normalized to Φ_0) applied to the SQUID loop and φ_b is the normalized flux due to additional fluxes generated by the normalized bias current i_1 and control currents i_2 and i_4 in the case of asymmetric inductances,

$$\varphi_b = \beta_L / 2 \cdot [(l_1 + l_2 - l_3 - l_4) \cdot i_1 / 2 + (3l_2 - l_1 - l_3 - l_4) \cdot i_2 / 4 + (l_1 + l_2 + l_4 - 3l_3) \cdot i_4 / 4], \quad (4)$$

where $l_k = L_k / L$.

We solve the equation (1) using a 5th order Runge Kutta method, together with equations (2a)–(4). The time derivatives $\partial_t \delta_k$ equal the normalized voltages $u_k = U_k / (I_0 R)$ across the four junctions, and from that we obtain the time averaged normalized voltages v_k . The time averaged voltage across the SQUID (between port 1 and 3) is $v_{\text{SQ}} = v_1 + v_2 = v_3 + v_4$. To record an IVC we typically start at zero current with initial conditions $\delta_k = u_k = 0$, let the system relax over 10^3 – 10^4 time units and then perform time averaging over 10^3 – 10^4 time units to obtain v_k . Then the current is changed by a small step and the procedure is repeated using the final values of δ_k and u_k of the previous step as the new initial conditions. The SQUID critical current is determined from i_1 vs. v_{SQ} characteristics by applying a voltage criterion $v_{\text{crit}} = 0.05$, which was chosen to be close to the experimental voltage criterion (see section 3.2).

The simulations discussed in this paper are for $\beta_C = 0$. We further use $l_k = 0.25$ for all k and $i_4 = 0$.

2.2. 4JJ SQUID behaviour for (nearly) symmetric junctions

To connect to the theoretical predictions shown in [28] we briefly address the symmetric 4JJSQ ($a_k = 1$) at $\beta_L = 1$. We first set the noise parameter to a very small value, $\Gamma = 10^{-6}$. For the perfectly symmetric 4JJSQ, $\Gamma = 0$ would produce solutions that are unstable against small perturbations.

Figure 2(a) shows the normalized critical current i_{c1} vs. φ_{ext} , calculated for five different values of $i_2 = 0, \pm 0.6$ and ± 1.2 . This graph agrees very well with figure 2(b) of [28]. The dependence i_{c1} vs. i_2 is shown in figure 2(b) for three values of $\varphi_{\text{ext}} = 0, 0.25$ and 0.5 and both polarities of i_1 . This graph can be compared with figure 3 of [28]. While the overall agreement is very good, there is a difference for $i_2 < -1.5$ (at $i_{c1} > 0$), where i_{c1} in our dynamic simulations shows an increase with decreasing i_2 , while i_{c1} in [28] continues to decrease, as indicated by the dashed blue and green lines in figure 2(b).

The differences can be understood from the IVC shown in figure 3(a) for $i_2 = -2$ and $\varphi_{\text{ext}} = 0$. The current i_1 was swept in steps of 0.02 using the sequence $0 \rightarrow 6 \rightarrow -6 \rightarrow 0$. The SQUID IVC v_{SQ} vs. i_1 shows a clear supercurrent up to $i_1 = 1.96$ at positive bias. However, when plotting the individual voltages v_k across junctions 1–4 vs. current i_1

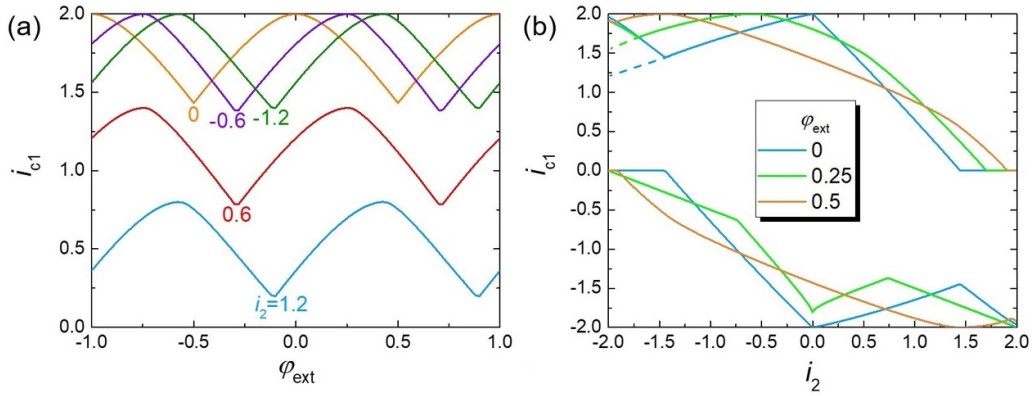


Figure 2. Simulations for comparison to results of [28] for a symmetric 4JJSQ ($a_k = 1$) with $\beta_L = 1$ and $\Gamma = 10^{-6}$. (a) i_{c1} vs. φ_{ext} for 5 different values of i_2 . (b) i_{c1} vs. i_2 for three different values of φ_{ext} . Differences to [28] occur in (b) at positive bias currents and i_2 values below -1.5 . In this region, dashed lines indicate i_{c1} vs. i_2 as obtained in [28].

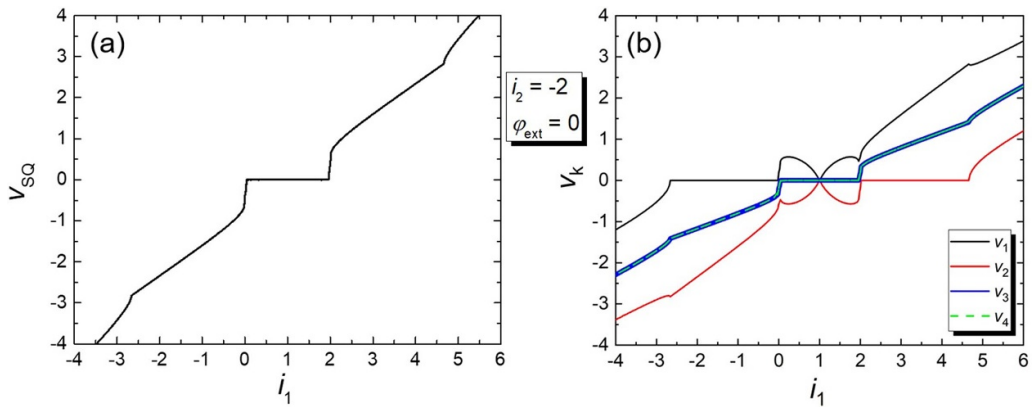


Figure 3. Simulations for a symmetric 4JJSQ ($a_k = 1$) with $\beta_L = 1$ and $\Gamma = 10^{-6}$, for $i_2 = -2$ and $\varphi_{\text{ext}} = 0$. (a) SQUID IVC v_{SQ} vs. i_1 . (b) Individual voltages of the four JJs, v_k vs. i_1 .

(figure 3(b)) one finds that for currents between 0.06 and 1.96 junctions 1 and 2 are in the resistive state with compensating voltages v_1 and v_2 , while the time-averaged voltages across junctions 3 and 4 are zero. This dynamic state could not be captured by the static analysis of [28].

As another remarkable dynamic feature, figure 4(a) shows IVCs (for $i_2 = 0$) for different $\varphi_{\text{ext}} = 0$ (black line), 0.25 (red line) and 0.5 (green line). For $\varphi_{\text{ext}} = 0$ and 0.25 the IVCs are hysteretic, although β_C was set to zero. One further notes in figure 4(a) that in the resistive state at fixed bias current the voltage v_{SQ} across the SQUID decreases with increasing flux, opposite to the case of a standard (2-JJ) dc SQUID and somewhat reminiscent to the case of a dc SQUID with nonzero β_C , if the LC-resonance-voltage of the SQUID is exceeded [33, 34]. This is more clearly visible in figure 4(b), which shows $v_{\text{SQ}}(\varphi_{\text{ext}})$ curves for different values of i_1 . Here we initialized the phases δ_k and voltages u_k with zero at a fixed value of i_1 and then swept φ_{ext} from either -1 to 1 or from 1 to -1 . For $i_1 = 1.5$, $v_{\text{SQ}}(\varphi_{\text{ext}})$ has maxima at $\varphi_{\text{ext}} = \pm 0.5$. With further increasing i_1 , those are converted into minima. From figure 4(a) we see that there is a resistive (downsweep) branch in the IVC also near integer values of φ_{ext} (with a return current to the zero-voltage state $i_{r1} = 0.88$ at $\varphi_{\text{ext}} = 0$), which

however, could not be stabilized for $i_1 < 1.7$ in our sweeps of φ_{ext} . For $i_1 = 1.7$ it appears only on the beginning of the sweep sequence. Also note that for $i_1 > 2.6$ there is a splitting of the $v_{\text{SQ}}(\varphi_{\text{ext}})$ curves near half-integer values of φ_{ext} . We did not investigate this feature further at this point.

While for $i_2 = 0$ at given bias current i_1 the time-averaged voltages v_k across all junctions are identical (not shown here), a difference shows up when inspecting the time-dependent voltages u_k , as displayed in figure 5 for $i_2 = 0$ and $i_1 = 1.8$. Figure 5(a) shows the case $\varphi_{\text{ext}} = 0$. Junctions 1 and 2, as well as junctions 3 and 4, oscillate in-phase. However, the voltage oscillations of the junctions 1 and 2 in the left and 3 and 4 in the right arm of the SQUID are out-of-phase, corresponding to a large circulating current around the SQUID. Consequently, the effective critical current i_{c1} is lowered compared to the static case, causing the hysteresis in the IVC. Note that for a symmetric two-junction SQUID the circulating current would be zero for $\varphi_{\text{ext}} = 0$.

In figure 4(a), we show that the hysteresis in the IVC decreases and eventually vanishes with increasing φ_{ext} . More precisely, the hysteresis disappears near $\varphi_{\text{ext}} = 0.314$. Figures 5(b) and (c) show $u_k(t)$ for $\varphi_{\text{ext}} = 0.25$ and 0.5, respectively. At $\varphi_{\text{ext}} = 0.25$ (figure 5(b)) the phase shift between the

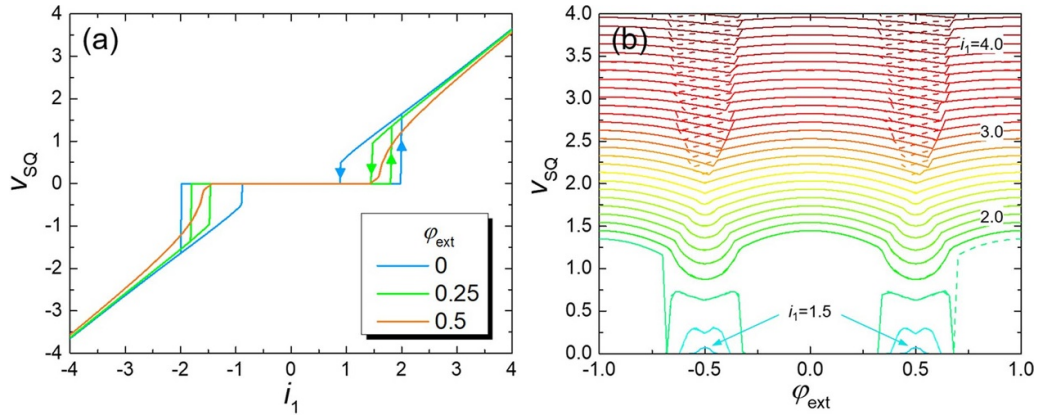


Figure 4. Simulations for a symmetric 4JJSQ ($a_k = 1$) with $\beta_L = 1$ and $\Gamma = 10^{-6}$ for $i_2 = 0$. (a) IVCs for different values of applied flux. Arrows indicate sweep direction. (b) Family of $v_{SQ}(\varphi_{ext})$ curves (solid lines: φ_{ext} from -1 to $+1$; dashed lines: φ_{ext} from $+1$ to -1) for different bias currents i_1 (from 1.4 to 4.3 in 0.1 steps).

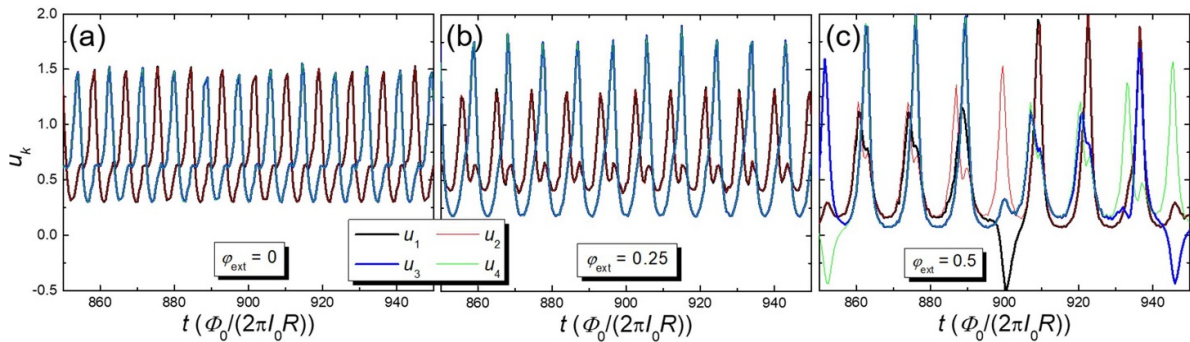


Figure 5. Simulation of time-dependent voltage oscillations of all 4 single JJs of a symmetric 4JJSQ ($a_k = 1$, $\beta_L = 1$ and $\Gamma = 10^{-6}$) at $i_2 = 0$ and $i_1 = 1.8$ for $\varphi_{ext} = 0$ (a), 0.25 (b) and 0.5 (c).

JJs in the left and right arm becomes smaller. If we increase φ_{ext} further to $\varphi_{ext} = 0.5$ (figure 5(c)), the system seems to become chaotic, and synchronization of JJs within the same SQUID arm gets lost. This chaotic regime seems to coincide with the region where the IVCs are no longer hysteretic. We also calculated families of $v_{SQ}(\varphi_{ext})$ curves for $i_2 = \pm 0.6$ and ± 1.2 (not shown). In all cases we observed instabilities in the $v_{SQ}(\varphi_{ext})$ patterns indicating that for the symmetric device chaotic regimes appear over a wide range of i_2 values.

Trivially, if the critical currents of one of the junctions in each arm of the SQUID were much bigger than the critical currents of the two other junctions one should return to the behaviour of a 2-junction SQUID. Thus, to investigate the quite unusual hysteresis in the IVCs (in the absence of JJ capacitance or heating effects) in some more detail we also show simulations for a somewhat asymmetric 4JJSQ with $a_1 = a_3 = 1.2$ and $a_2 = a_4 = 1$. The parameters are chosen such that the left and right arm of the SQUID remain symmetric.

Figure 6(a) shows by the red line i_{c1} vs. φ_{ext} for the asymmetric case in comparison to the symmetric case (black line). In both cases, the critical current has a maximum $i_{c1,max} = 2$ at $\varphi_{ext} = 0$ and minima $i_{c1,min}$ at $\varphi_{ext} = \pm 0.5$, like for a symmetric 2-junction SQUID. But one notes that the modulation depth $(i_{c1,max} - i_{c1,min})/i_{c1,max}$ of the asymmetric 4JJSQ is larger than for the symmetric 4JJSQ and closer to the modulation depth

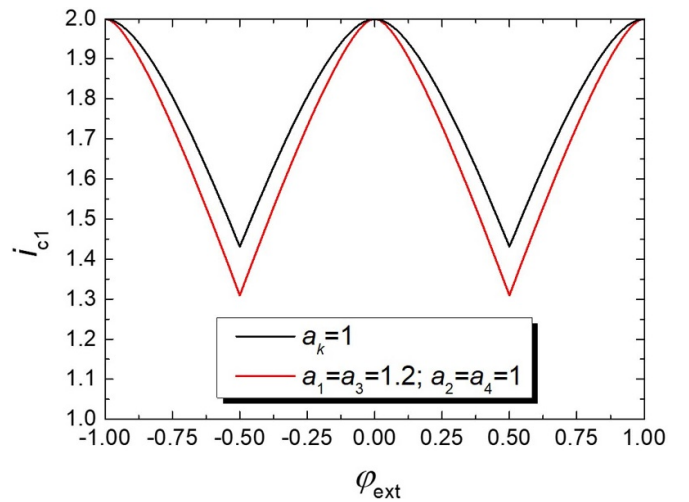


Figure 6. Simulations ($\beta_L = 1$, $\Gamma = 10^{-6}$, $i_2 = 0$), comparing $i_{c1}(\varphi_{ext})$ -curves for a symmetric (black line) and slightly asymmetric (red line) 4JJSQ.

of $1/2$ which would be obtained for a symmetric 2-junction SQUID with $\beta_L = 1$.

Figure 7(a) shows IVCs for the asymmetric 4JJSQ for $\varphi_{ext} = 0$ (maximum i_{c1}) and 0.5 (minimum i_{c1}). For $\varphi_{ext} = 0$

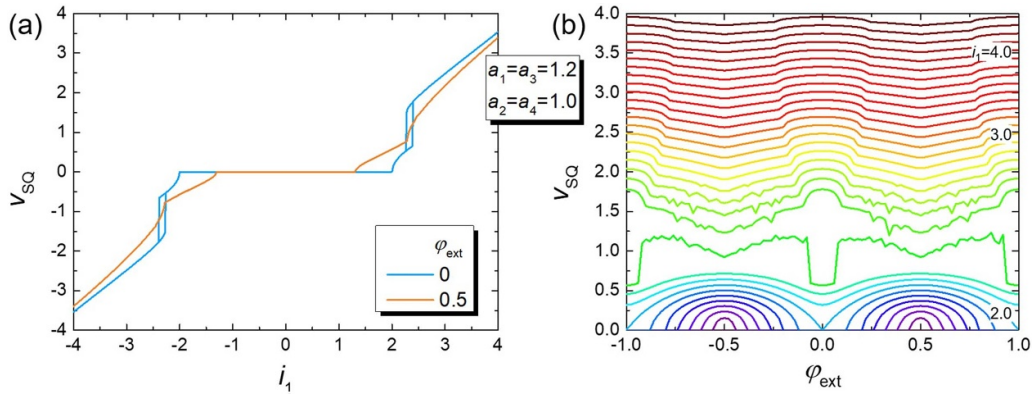


Figure 7. Simulations ($\beta_L = 1$ and $\Gamma = 10^{-6}$, $i_2 = 0$) for slightly asymmetric 4JJSQ ($a_1 = a_3 = 1.2$; $a_2 = a_4 = 1$). (a) IVCs at two different values of applied flux. (b) Family of $v_{SQ}(\varphi_{ext})$ curves for different bias currents i_1 (from 1.4 to 4.4 in 0.1 steps). φ_{ext} is swept from -1 to 1 .

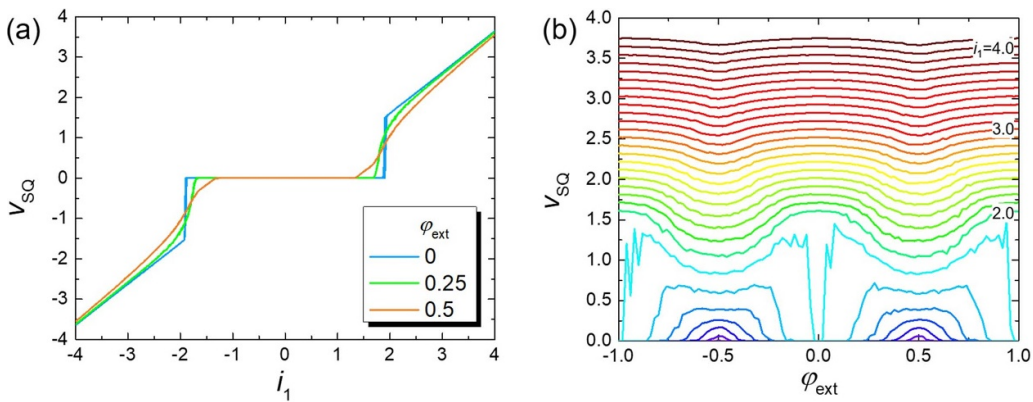


Figure 8. Simulations for a symmetric 4JJSQ ($a_k = 1$) with $i_2 = 0$, $\beta_L = 1$ and $\Gamma = 4.4 \cdot 10^{-3}$. (a) Simulated IVCs for different values of applied flux. (b) Family of $v_{SQ}(\varphi_{ext})$ curves for different values of bias current i_1 (from 1.4 to 4.1 in 0.1 steps). φ_{ext} is swept from -1 to 1 .

the critical current $i_{c1} = 2$, i.e. the two weaker JJs 2 and 4 (with $a = 1$) are switching to the resistive state. With further increasing i_1 , we find a jump to higher v_{SQ} at $i_1 = 2.4$, which means that now also JJs 1 and 3 (with $a = 1.2$) become resistive. We also find for the slightly asymmetric 4JJSQ a hysteretic IVC for $\varphi_{ext} = 0$; however, this is smaller than for the symmetric 4JJSQ, and it is also suppressed with increasing φ_{ext} . In the resistive state one observes a crossover between the two IVCs at $\varphi_{ext} = 0$ and 0.5 .

Figure 7(b) displays for the slightly asymmetric 4JJSQ a family of $v_{SQ}(\varphi_{ext})$ curves for different bias currents i_1 . Like for the symmetric 4JJSQ, at low bias currents the voltage maximum occurs at half-integer values of φ_{ext} . With increasing i_1 one observes the crossover to the state where the maxima of v_{SQ} vs. φ_{ext} occur at integer values of φ_{ext} . Also note, that near the crossover the v_{SQ} vs. φ_{ext} curves look noisy. This is because of the small hysteresis visible in the IVCs.

Finally, for the symmetric device, we also address the case of higher thermal noise. We take $\Gamma = 4.4 \cdot 10^{-3}$, a value, which we find for our experimental 4JJSQ discussed below. Figure 8(a) shows IVCs for $\varphi_{ext} = 0, 0.25$ and 0.5 . The large hysteresis observed for $\Gamma = 10^{-6}$ has nearly vanished, and we observe a low-bias region where the voltage at $\varphi_{ext} = 0.5$ is higher than the voltage for lower values of φ_{ext} . This can also be seen in the v_{SQ} vs. φ_{ext} curves displayed in figure 8(b),

where one observes the crossover in the position of voltage maxima from half-integer to integer values of φ_{ext} at voltages near 1. Also note that the voltage jumps associated with the splitting of the $v_{SQ}(\varphi_{ext})$ curves at high bias currents are no longer observable.

3. Fabrication and measurement results

3.1. Fabrication and design

The 4JJSQs with deep submicron sandwich-type trilayer SNS JJs with Nb electrodes and HfTi barrier were fabricated using an established Nb planar fabrication technology. This is based on magnetron sputtering deposition on 3 inch Si wafers with 300 nm thermally oxidized SiO_2 , electron beam lithography to ensure high alignment precision for nanopatterning of the small features of our SQUIDS and a chemical-mechanical polishing step to planarize the insulating SiO_2 layer between the Nb base and the Nb wiring layer and to open contact windows between the Nb top layer and Nb wiring layer. Those technologies are available at the clean room center at PTB Braunschweig and have been applied before to the fabrication of JJ-based circuits [35–38], including complex and advanced nanoSQUID layouts, such as gradiometers [39] and 3-axis vector nanoSQUIDS [40] and for auxiliary components such

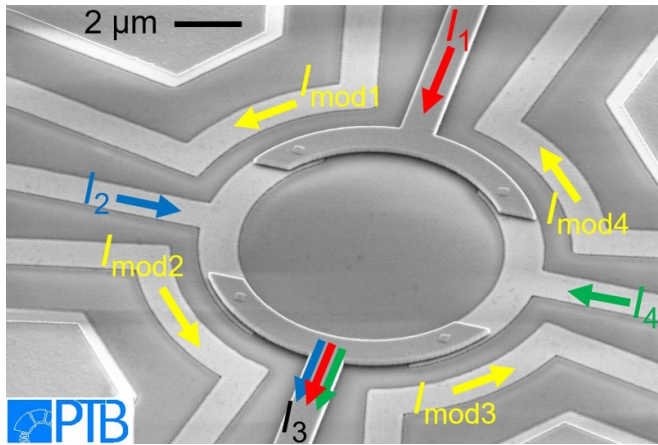


Figure 9. Scanning electron microscopy image of a 4JJSQ. Two superconducting quadrants in the Nb base layer are connected via four JJs to two quadrants in the Nb wiring layer. The bias current I_1 , drain current I_3 , control currents I_2 and I_4 and modulation currents $I_{\text{mod}1}$ to $I_{\text{mod}4}$ are indicated by arrows. The voltage across the 4JJSQ is measured between the ports 1 and 3 for bias current I_1 and drain current I_3 , respectively.

as pick-up and feedback coils. Since the fabrication technology is not the focus of this paper, we refer to [41] for the detailed fabrication technology.

We fabricated dc SQUIDS with four SNS JJs with nominal lateral JJ size of $300 \text{ nm} \times 300 \text{ nm}$ (figure 9) and a normal conducting $\text{Hf}_{\text{wt}50\%}\text{Ti}_{\text{wt}50\%}$ (HfTi) barrier with a thickness of 26 nm. The superconducting Nb loop is constructed as two quadrants in the 160 nm thick Nb base layer which are connected via the four JJs to two more quadrants in the Nb wiring layer, which has a thickness of 200 nm. The applied magnetic flux φ_{ext} to the SQUID can be provided by the modulation currents $I_{\text{mod},i}$ ($i = 1-4$) through four inductively coupled modulation lines in the Nb base layer, which are designed to be in a close distance (with a nominal $0.9 \mu\text{m}$ gap) to the four SQUID loop segments. The SQUID loop was designed to have an inner diameter of $8.0 \mu\text{m}$ with $1.1 \mu\text{m}$ linewidth for the Nb base and $8.1 \mu\text{m}$ diameter with $0.9 \mu\text{m}$ line width in the wiring layer.

3.2. Basic SQUID characterization

All measurement data shown here were taken at liquid He temperature ($T = 4.2 \text{ K}$) and we used the current I_1 , flowing from the top across the SQUID loop to the drain (bottom; see figure 9) as the bias current. The SQUID voltage V_{SQ} was measured between ports 1 and 3. The modulation current $I_{\text{mod}1}$ was used to inductively couple magnetic flux Φ_1 to the SQUID loop, via the mutual inductance $M_1 = \Phi_1/I_{\text{mod}1}$. The control current I_2 , flowing from the left to the drain, was used to shift the interference patterns. We always kept $I_4 = 0$, and accordingly, $I_3 = I_1 + I_2$. Also, we limit the results presented below to one exemplary 4JJSQ, since the other investigated 4JJSQs showed similar behaviour.

The IVCs $V_{\text{SQ}}(I_1)$, with $I_{\text{mod}1}$ adjusted to obtain maximum critical current $I_{\text{c}1,\text{max}}$ and minimum critical current $I_{\text{c}1,\text{min}}$ are shown in figure 10(a) for the 4JJSQ with $I_2 = 0$ and

$37.5 \mu\text{A}$. These IVCs, as well as all others we obtained, are nonhysteretic. For $I_2 = 0$ the maximum critical current is $80 \mu\text{A}$, which corresponds to $I_0 \approx 40 \mu\text{A}$ and a critical current density $j_0 \approx 44 \text{ kA cm}^{-2}$. For the noise parameter we find $\Gamma \approx 4.4 \cdot 10^{-3}$ at 4.2 K . Further, we find the best overall agreement between the shapes of the experimental and simulated IVCs for $i_2 = 0$ by using $I_0R = 15 \mu\text{V}$.

We show in figure 10(b) the voltage oscillation $V_{\text{SQ}}(I_{\text{mod}1})$ for the 4JJSQ (with $I_2 = 0$) at $I_1 = 80 \mu\text{A}$. From the oscillation period (current $I_{\text{mod}1,0}$ required to couple one flux quantum Φ_0 to the SQUID) we determine the inverse mutual inductance $1/M_1 = I_{\text{mod}1,0}/\Phi_0 = 1.95 \text{ mA}/\Phi_0$ ($M_1 = 1.06 \text{ pH}$) between the corresponding modulation line and the 4JJSQ. The maximum modulation voltage of our 4JJSQ is $9 \mu\text{V}$ (cf figure 10(b)) and the derived maximum transfer coefficient is $V_{\Phi} \approx 50 \mu\text{V}/\Phi_0$. Using the simulation software 3D-MLSI, to calculate the supercurrent density distribution based on the London equations [42] for the given geometry of our device and with a London penetration depth $\lambda_L = 70-80 \text{ nm}$ for our Nb thin films, we obtain for the mutual inductance $M_1 = 1.12 \text{ pH}$, which is in good agreement with the value $M_1 = 1.06 \text{ pH}$ determined experimentally from figure 10(b). For the SQUID inductance we calculate with 3D-MLSI $L = 17.0 \text{ pH}$, leading to an estimated screening parameter $\beta_L = 2I_0L/\Phi_0 \approx 0.66$. From direct simulations (see below) we obtain $\beta_L = 0.65$ and $L = 16 \text{ pH}$, which is in very good agreement.

To work with dimensionless quantities for comparing our measurement results with calculations from [28] and with our simulations based on the mathematical model described in section 2, we normalize the currents I_1 and I_2 to I_0 and the modulation current $I_{\text{mod}1}$ to $I_{\text{mod}1,0} = \Phi_0/M_1$. The voltages are normalized to $I_0R = 15 \mu\text{V}$. We denote normalized quantities by lower case letters i and v . $\varphi_1 = I_{\text{mod}1}/I_{\text{mod}1,0} = \Phi_1/\Phi_0$ is the normalized applied flux (modulation current).

For the simulations shown below we use asymmetry parameters $a_1 = 1.05$ and $a_4 = 0.95$, so that we have $a_1 + a_4 = 2$ for the weakest JJs in both SQUID arms. We further use $a_2 = 1.15$ and $a_3 = 5$ and $\beta_L = 0.65$. These values have been obtained by matching $i_{\text{c}1}$ vs. φ_1 curves for $i_2 = 0$ and $i_2 = 1.25$, as well as IVCs for $i_2 = 0$ and φ_1 chosen so that the positive critical current was at a maximum or a minimum. Parameters a_1 to a_4 , as well as β_L were varied in steps of 0.05. For the asymmetry parameter a_3 we can give only a lower limit of 4 and for convenience set this parameter to 5. We briefly note here that, by inspecting IVCs for $i_4 = 0$ only, in the absence of measurements of the individual voltages v_k , we could have exchanged the values of a_3 and a_4 without changing the results. However, using the measured individual junction voltages, as well as using measurements with nonzero values of the current i_4 , we find JJ3 to be the junction with significantly higher asymmetry parameter. In experiment the threshold voltage to determine the critical current was $1 \mu\text{V}$, translating to a normalized voltage criterion of about 0.07 to determine $i_{\text{c}1}$ in our simulations. Finally, we note that to match experimental $i_{\text{c}1}(\varphi_1)$ or $v_{\text{SQ}}(\varphi_1)$ curves with simulations, the experimental I_{mod} -axes needed to be adjusted typically by an offset of $0.05-0.1 \text{ mA}$ to account for residual fields of $\approx 1-2 \mu\text{T}$ in the cryostat.

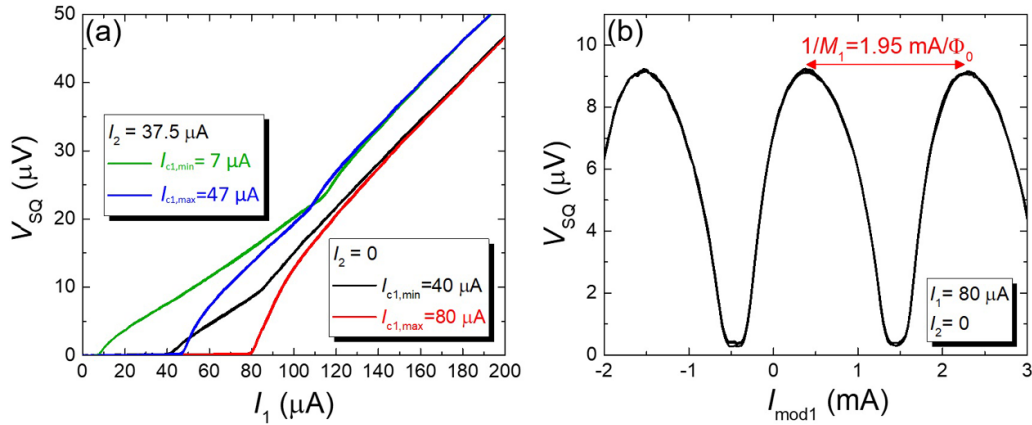


Figure 10. Experimental results for the 4JJSQ at 4.2 K. (a) IVCs with I_{mod1} adjusted to achieve maximum ($I_{c,max}$) and minimum ($I_{c,min}$) critical current for $I_2 = 0$ and $37.5 \mu A$. (b) Voltage vs. modulation current for $I_2 = 0$ (chosen to obtain maximum voltage modulation amplitude).

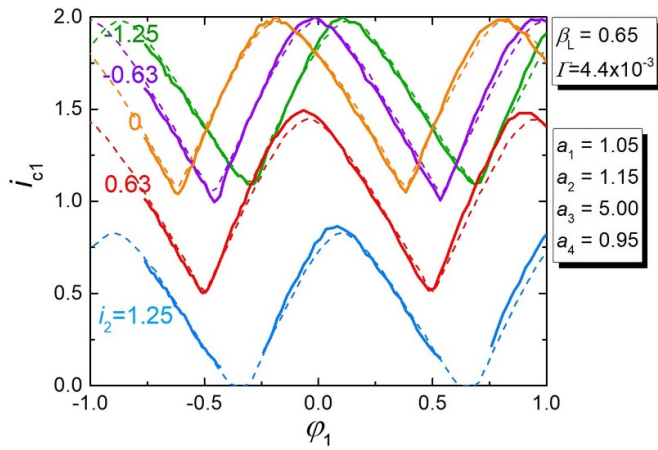


Figure 11. Measured (solid lines) and simulated (dashed lines) $i_{c1}(\phi_1)$ curves of the 4JJSQ for 5 different control currents i_2 . The boxes to the right indicate the values for the parameters used in the simulations.

Figure 11 shows by solid lines the measured quantum interference patterns $i_{c1}(\phi_1)$ of our 4JJSQ together with the corresponding simulated curves (dashed lines). Here we measured IVCs for 101 different values of the modulation current, varying between $I_{mod1} = -1.48 \text{ mA}$ and 2.40 mA , at 5 different values of the applied control current i_2 , which were chosen to be between -1.25 and 1.25 .

As predicted by the model described in [28], the quantum interference patterns in figure 11 are not only shifted to lower critical currents, but also along the ϕ_1 -axis while applying a positive control current ($i_2 > 0$). For negative control currents ($i_2 < 0$) the patterns are shifted only along the ϕ_1 -axis, which agrees with the theoretical model, too. Compared to [28] and to our simulations for symmetric 4JJSQs (cf figure 2(a)) we observe a shift of all quantum interference patterns to the left, which is due to the asymmetry in the junction critical currents of our device.

Now, we compare our simulation results to IVCs measured at different values of applied flux and $i_2 = 0$. The measured

curves are presented in figure 12(a), whereas the simulated curves are shown in figure 12(b). In general, there is a good agreement between the measurement and the simulation. Particularly, the measured critical current values and the ‘bends’ (abrupt changes in the slope) observed in the IVCs for different values of applied flux could be reproduced by simulations.

An explanation for the bending of the IVCs can be found by having a closer look at the voltages v_k across the four individual junctions, shown in figure 13 for $i_2 = 0$. The left panels (a), (c) show measurements and the right panels (b), (d) show simulations. The upper panels (a), (b) show $v_k(i_1)$ at maximum critical current (at $\phi_1 = -0.17$), and the lower panels are for minimum critical current (at $\phi_1 = 0.41$). In both cases, JJ3 stays in the zero-voltage state. The voltage v_1 across JJ1 equals v_4 as long as JJ2 is in the zero-voltage state, while v_1 is close to v_2 as soon as v_2 becomes nonzero. This transition marks the bends in the IVCs shown in figure 12, where the voltages are the sum of the JJs in the right and left arm, respectively.

With respect to the IVCs we briefly mention that also for nonzero values of i_2 we found a very good agreement between experiment and simulation. However, neither in experiment nor in simulation we found hysteretic IVCs for our strongly asymmetric device, as we found in our simulations for the (nearly) symmetric 4JJSQ, cf figures 4–6.

Figure 14 shows measured (figure 14(a)) and simulated (figure 14(b)) families of $v_{SQ}(\phi_1)$ curves for $i_2 = 0$. Here, we varied the bias current i_1 in steps of 0.1 from 1 to 4 for positive bias and from -1 to -4 for negative bias.

The v_{SQ} vs. ϕ_1 curves show a point-symmetric behaviour and for $|i_1| \lesssim 1.5$ one observes the voltage maxima at half-integer values of the applied flux (shifted due to the asymmetric JJs), similar to 2-junction SQUID behaviour. For higher values of the bias current $|i_1|$, the maxima of the $v_{SQ}(\phi_1)$ curves are gradually shifting further to the left and right, for positive and negative i_1 , respectively. The simulations are in good agreement with the experimental data. As we neglected inductance and resistance asymmetries in the simulations, the above-described shifts in the voltage maxima are attributed to critical current asymmetries only. Note that in contrast to the

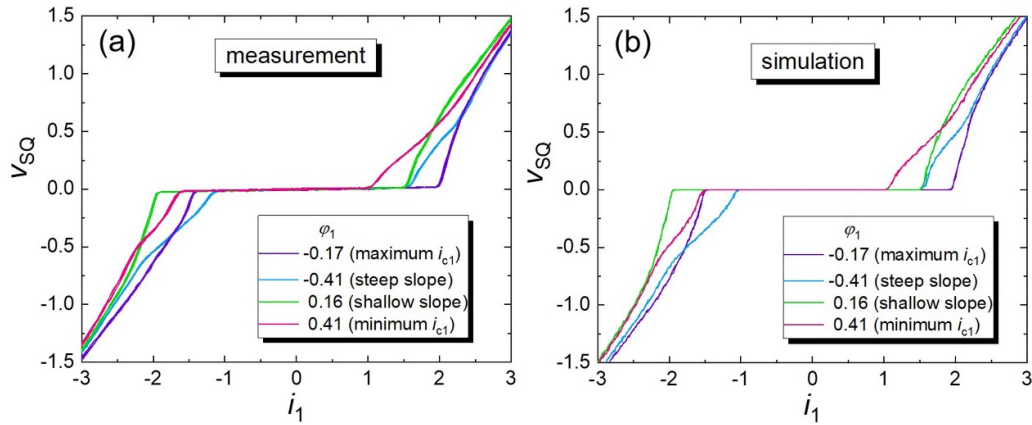


Figure 12. (a) Measured and (b) simulated (same parameters as in figure 11) IVCs for $i_2 = 0$ and different values of applied flux to reach either maximum or minimum i_{c1} or to stay on the steep or shallow slope of the $i_{c1}(\varphi_1)$ pattern (for $i_1 > 0$; cf figure 11).

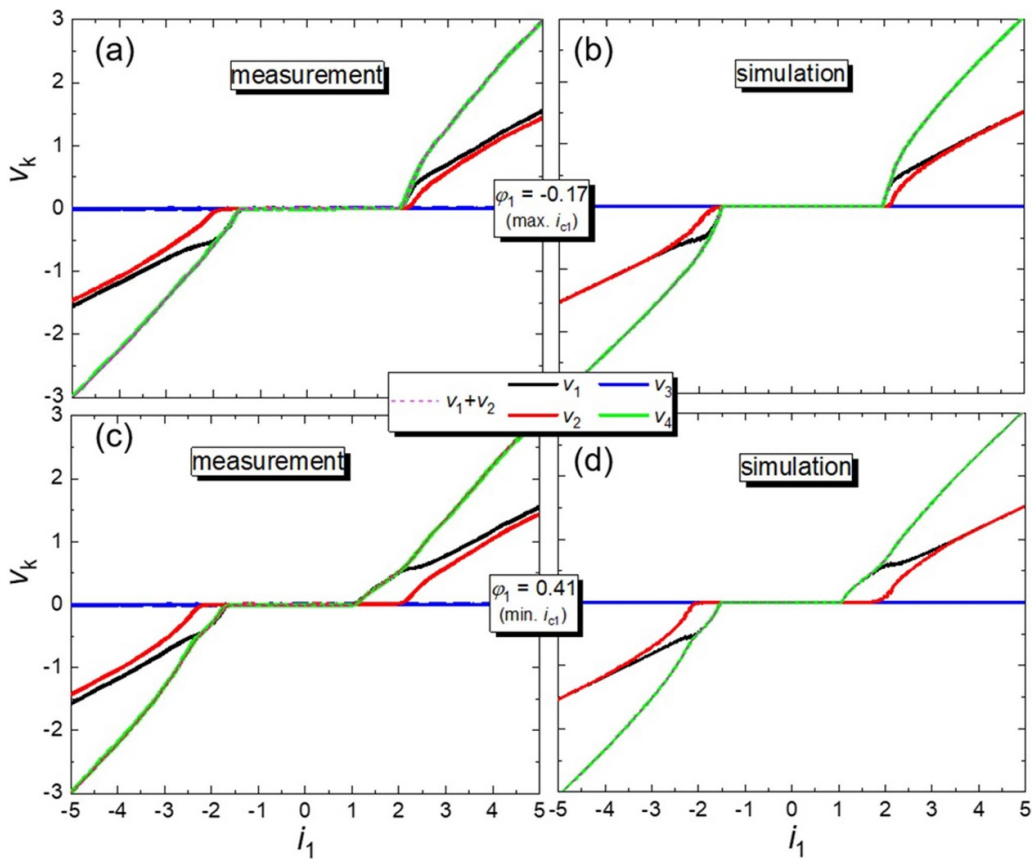


Figure 13. (a), (c) Measurement and (b), (d) simulation (same parameters as in figure 11) of the voltages $v_k(i_1)$ of the individual four junctions of the 4JJSQ for $i_2 = 0$ and an applied flux leading to maximum (a), (b) and minimum (c), (d) critical current (solid lines). Dashed lines show the total voltage across the SQUID.

simulated $v_{SQ}(\varphi_{ext})$ families shown in figures 4, 7 and 8, we do not observe an abrupt crossover of the position of the voltage maxima from half-integer to integer values of the applied normalized flux. Further note that in contrast to the case of the simulated $v_{SQ}(\varphi_{ext})$ families for the symmetric 4JJSQ with comparable noise parameter, the v_{SQ} vs. φ_1 curves look much less noisy close to $v_{SQ} \approx 1$, which is consistent with the missing hysteresis in the IVCs of our asymmetric device.

Figure 15 shows measured (figure 15(a)) and simulated (figure 15(b)) $v_{SQ}(\varphi_1)$ curves for $i_2 = 0$ and ± 0.95 while the bias current is chosen to obtain maximum voltage modulation amplitude. We observe a shift of the curves along the φ_1 -axis while applying a positive control current ($i_2 = 0.95$) as well as negative control currents ($i_2 = -0.95$) compared to the case of $i_2 = 0$. In contrast to the symmetric device, no instabilities appear in the curves.

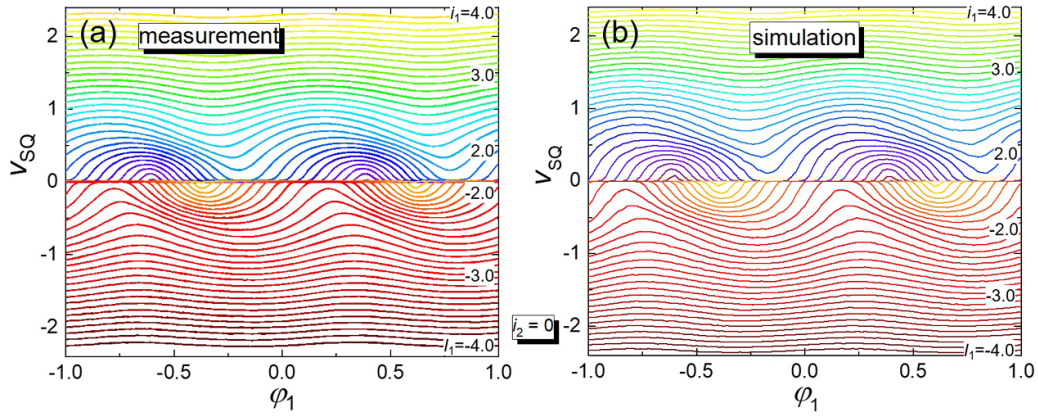


Figure 14. Families of (a) measured and (b) simulated (same parameters as in figure 11) $v_{SQ}(\varphi_1)$ curves for different values of the bias current i_1 ($|i_1|$ from 1.0 to 4.0 in 0.1 steps) and for control current $i_2 = 0$.

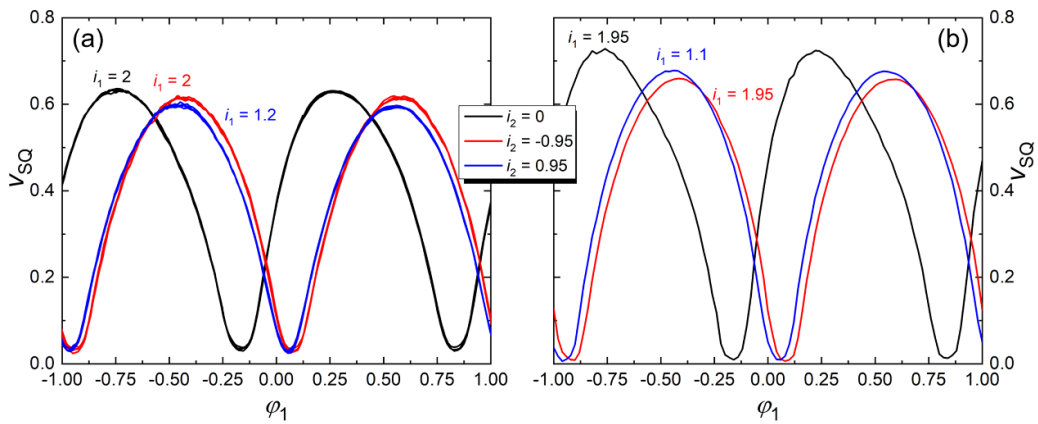


Figure 15. (a) Measured and (b) simulated $v_{SQ}(\varphi_1)$ curves for different values of control current i_2 and bias current i_1 (chosen to obtain maximum voltage modulation amplitude).

3.3. Critical current vs. i_2

Figure 16 displays the measured (a) and simulated (b) critical currents i_{c1} vs. control current i_2 for both polarities of i_{c1} and different values of applied flux (taking into account that for $i_2 = 0$ the $i_{c1}(\varphi_1)$ curves have their maximum at $\varphi_1 = -0.17$ for $i_{c1} > 0$, and at 0.16 for $i_{c1} < 0$). The agreement between the measured and the simulated curves is very good and, like for the symmetric case (cf figure 2(b)), we observe both in experiment and simulation an increase of the critical current for positive bias, for $i_2 < -1.5$ and φ_1 adjusted to be near the $i_{c1}(\varphi_1)$ maximum for $i_2 = 0$.

The upper panel of figure 17 displays experimental (a) and simulated (b) IVCs $v_{SQ}(i_1)$ for $i_2 = -2$ and the same three values of φ_1 that were chosen for the $i_{c1}(i_2)$ curves in figure 16 for $i_{c1} > 0$. Again, the agreement between experiment and simulation is very good. The lower panel of figure 17 shows measured (c) and simulated (d) individual junction voltages $v_k(i_1)$ for $\varphi_1 = 0.31$ and $i_2 = -2$. Like for the symmetric case, cf figure 3(b), the simulations yield a state where the junctions in the left arm are resistive, with opposite dc voltages, while the junctions in the right arm remain in their zero-voltage state. This state is also realized in the experimental device.

3.4. Current-phase relation

As explained in [28] the current-phase relation $F(\delta)$ of junctions 1 and 2 can be reconstructed from measurements of the critical current $i_{c1}(\varphi_1, i_2)$. For a given value of i_2 one determines the flux value φ_1 where $i_{c1}(\varphi_1)$ has a maximum. This constitutes the curve $\varphi_{1, \max}(i_2)$ which encodes the CPR of JJ1 for $i_2 > a_2 - a_1$ and the CPR of JJ2 for $i_2 \leq a_2 - a_1$.

For junction 2 the phase δ_2 is found from:

$$\delta_2 = -2\pi\varphi_{1, \max} - \pi\beta_L i_2/4 + \mu, \quad (5)$$

and the normalized CPR $F_2(\delta_2)/I_0$ is obtained via:

$$F_2(\delta_2)/I_0 = j_2 = i_2 + a_1. \quad (6)$$

The phase μ is a constant and can, e.g. be determined by demanding $F_2(0) = 0$.

From equation (3), using the definition of j_{SQUID} and further assuming sinusoidal CPR's and under the assumption that junction 4 is at its critical current we can also give an analytic expression for μ ,

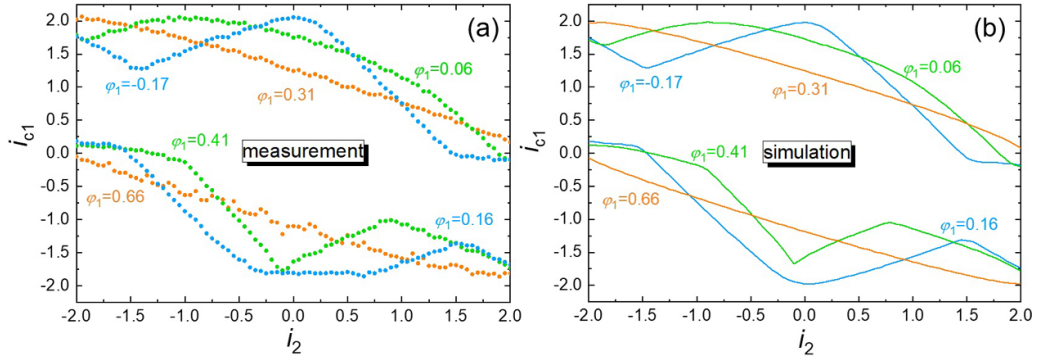


Figure 16. Comparison between (a) measured and (b) simulated (same parameters as in figure 11) $i_{c1}(i_2)$ curves for different values of applied flux. The blue curves correspond to applied flux values which yield maximum i_{c1} in the $i_{c1}(\varphi_1)$ curves for $i_2 = 0$. For the green and orange curves, φ_1 is increased by approximately $1/4$ and $1/2$, respectively.

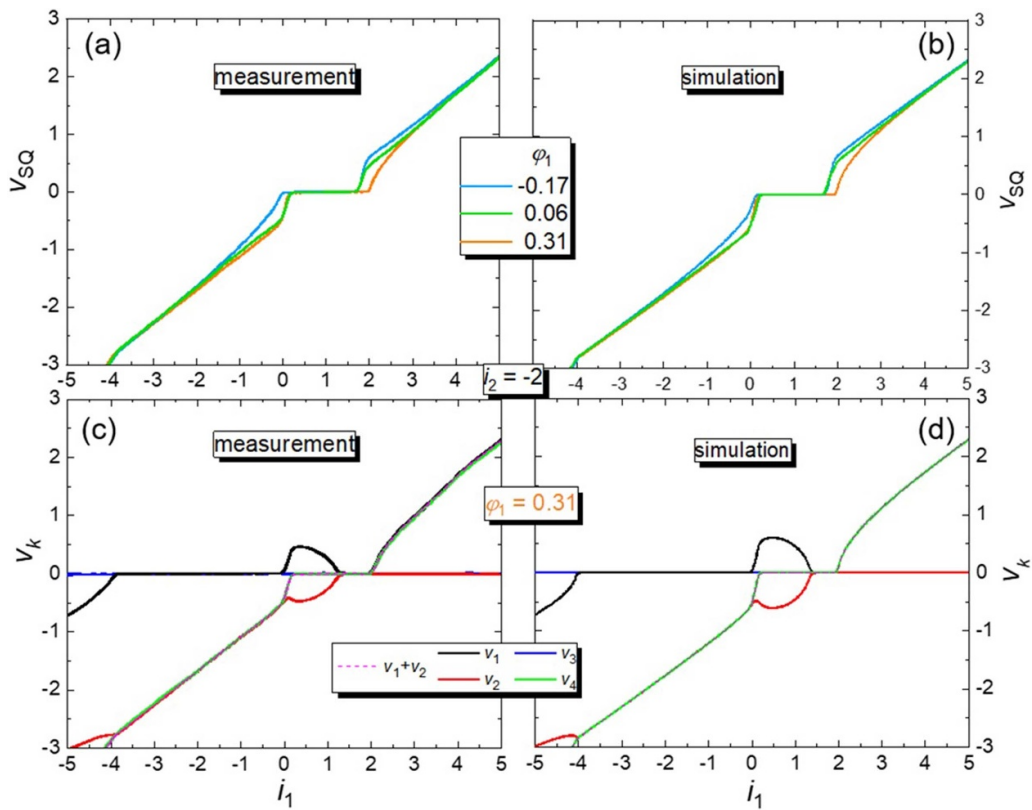


Figure 17. Measured (a) and simulated (b) IVCs $v_{SQ}(i_1)$ for $i_2 = -2$ and three values of φ_1 and measured (c) and simulated (d) individual junction voltages $v_k(i_1)$ for $i_2 = -2$ and $\varphi_1 = 0.31$. For the simulations, same parameters as in figure 11 were used.

$$\mu = a_4/a_3 - \pi\beta_L(a_1 - a_4)/2. \quad (7)$$

For junction 1 one makes the replacements $i_2 \rightarrow -i_2$, $a_1 \leftrightarrow a_2$, $\delta_2 \rightarrow \delta_1$, and for μ one finds:

$$\mu = a_4/a_3 - \pi\beta_L(a_2 - a_4)/2. \quad (8)$$

Figure 18(a) shows a measured contour plot $i_{c1}(\varphi_1, i_2)$. Here, we measured IVCs for 52 different values of φ_1 from -0.9 to 1 for 81 different values of i_2 between -2 and 2 . $\varphi_{1,\max}(i_2)$ is indicated by the pink symbols for φ_1 between -0.25 and 0.3 and for both polarities of i_2 . The

reconstructed normalized CPRs $F_i(\delta_i)/(a_i I_0)$ are shown in figure 19(a) for junction 1 and in figure 19(b) for junction 2. In the graphs we also plotted by lines the sinusoidal dependences. For the phase shift we used $\mu = -0.22$ for junction 1 and $\mu = -0.12$ for junction 2, to fulfil $F_1(0) = F_2(0) = 0$. Apparently, the data points are compatible with a sinusoidal CPR, although the error bars are large. Using the sinusoidal CPRs we also inverted equations (5) and (6) and show the resulting $\varphi_{1,\max}(i_2)$ curves as solid white lines in figure 18(a).

Finally, for completeness and in order to further test the evaluation method we applied the same procedure for the simulated $i_{c1}(\varphi_1, i_2)$ curves, where by ansatz we have sinusoidal

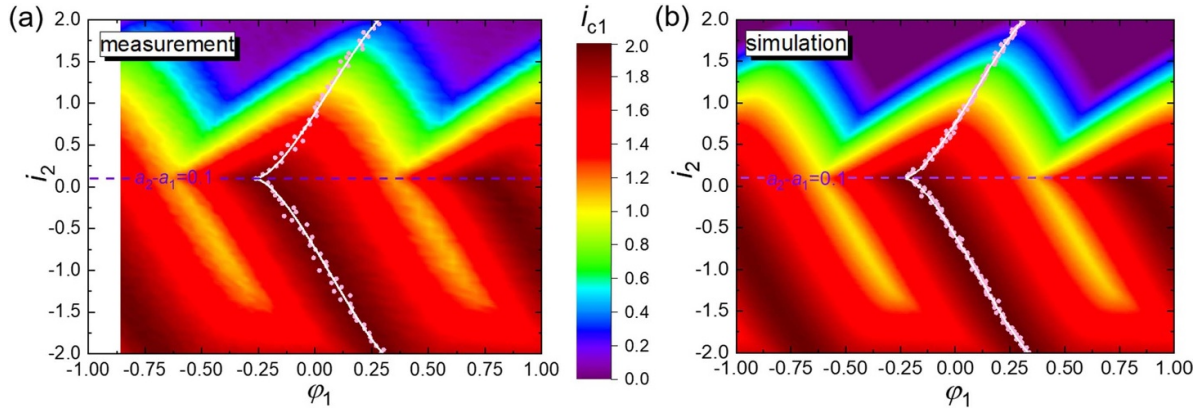


Figure 18. (a) Measured and (b) simulated (same parameters as in figure 11) contour plot $i_{c1}(\varphi_1, i_2)$ for the 4JJSQ. Pink dots indicate the maxima of the i_{c1} vs. φ_1 patterns at fixed values of i_2 , i.e. $\varphi_{1,\max}(i_2)$. The white solid lines are calculated by inverting equations (5) and (6) for sinusoidal CPRs for junctions 1 and 2. Values of $i_2 > a_2 - a_1$ are for junction 1 while values of $i_2 \leq a_2 - a_1$ are for junction 2.

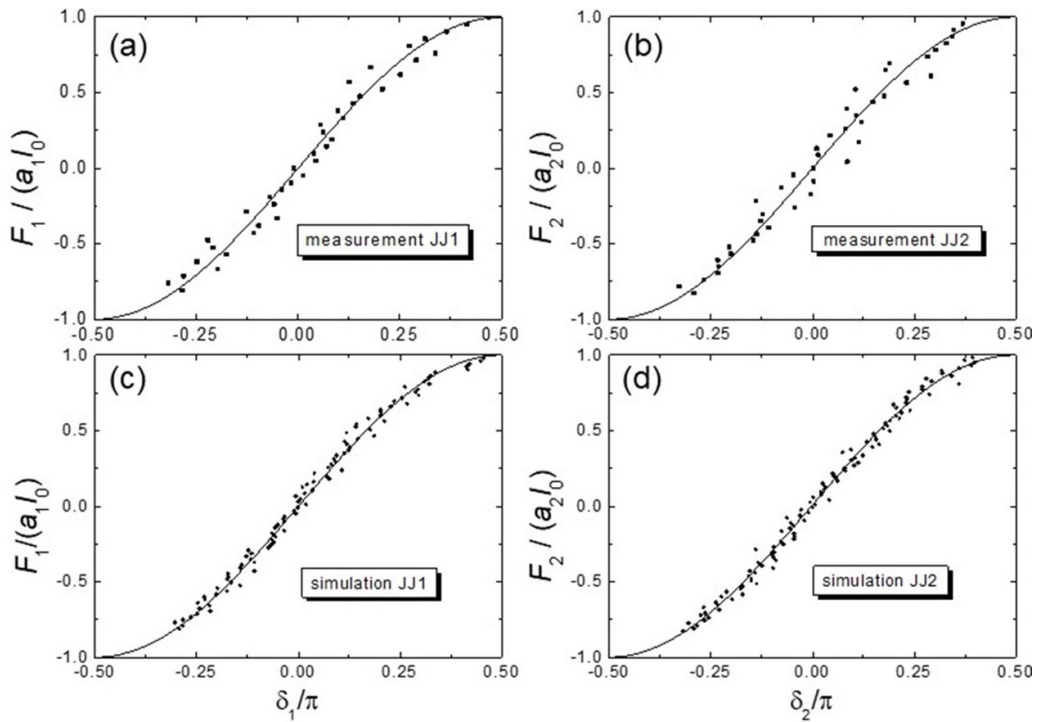


Figure 19. CPRs of JJ1 (a) and JJ2 (b), extracted from measured $\varphi_{1,\max}(i_2)$ data. CPRs of JJ1 (c) and JJ2 (d), extracted from the simulated $\varphi_{1,\max}(i_2)$ data. Lines correspond to sinusoidal CPRs $F_1/(a_1 I_0) = \sin \delta_1$ and $F_2/(a_2 I_0) = \sin \delta_2$.

CPRs. Figure 18(b) shows the corresponding contour plot $i_{c1}(\varphi_1, i_2)$. In the calculations both φ_1 and i_2 were varied in steps of 0.02.

Figures 19(c) and (d) show the extracted CPRs, where we used $\mu = 0$ for JJ1 and $\mu = 0.1$ for JJ2 to fulfil $F_1(0) = F_2(0) = 0$. Those values are close to $\mu = -0.01$ and 0.09, found from equations (7) and (8), respectively. We further note that the experimental data yield values for μ that are shifted by $\Delta\mu = -0.22$ relative to the simulated ones. This may indicate that a_3 of the experimental device is much larger than the value of 5 used for simulation. Indeed, $a_3 \rightarrow \infty$ would roughly lead to the observed value of $\Delta\mu$.

4. Conclusions

Motivated by the fact that the multi-terminal, multi-junction SQUID, suggested and realized for the SQUID-on-tip configuration, is also an interesting concept for other highly miniaturized SQUIDs we fabricated four-terminal, four-junction SQUIDs, using Nb SNS-junctions with a HfTi barrier. Like the conventional two-junction dc SQUID, also this device can be very well modelled using RCSJ-type equations, and we see that the static behaviour is similar to that of the 4-junction SQUID-on-tip. Particularly in the resistive state the dynamics of the device can strongly differ from the dynamics of a

conventional dc SQUID, involving various phase-locked and chaotic states if the 4-junction SQUID is symmetric. We have addressed several examples. While the symmetric device may be interesting for studies of nonlinear dynamics, the appearance of chaos and of instabilities in the current–voltage characteristics and the voltage–flux patterns is clearly detrimental for SQUID magnetometry. However, these effects have disappeared in the *asymmetric* 4-junction SQUID studied experimentally. Under this condition, as judged from the transport characteristics, the multi-terminal, multi-junction configuration is a promising geometry, allowing for a stable *in-situ* control over shifting interference patterns. This may become particularly important when it comes to pushing the limits of miniaturization, which will make it increasingly difficult to optimally flux-bias the conventional two-junction dc SQUID. However, it remains to be investigated, how the 4-junction dynamics imprints on the noise properties of the SQUID.

Data availability statement

The data that support the findings of this study are available upon reasonable request from the authors.

Acknowledgments

The authors thank K Störr, M Petrich, R Gerdau and P Hinze for their help throughout the wafer fabrication and support at the SEM equipment.

We gratefully acknowledge financial support by the Deutsche Forschungsgemeinschaft (DFG) (KI 698/3-2, KO 1303/13-2), by the European Commission under H2020 FET Open grant ‘FIBsuperProbes’ (Grant No. 892427) and by the COST action NANOCOHYBRI (CA16218). This work was partially funded from the EMPIR programme (Project ParaWave 17FUN10) co-financed by the Participating States and from the European Union’s Horizon 2020 research and innovation programme.

ORCID iDs

S Wolter  <https://orcid.org/0000-0001-7702-6813>
 D Koelle  <https://orcid.org/0000-0003-3948-2433>
 R Kleiner  <https://orcid.org/0000-0002-2819-9774>
 O Kieler  <https://orcid.org/0000-0001-5193-8910>

References

- [1] Vasyukov D *et al* 2013 A scanning superconducting quantum interference device with single electron spin sensitivity *Nat. Nanotechnol.* **8** 639–44
- [2] Wernsdorfer W 2001 Classical and quantum magnetization reversal studied in nanometersized particles and clusters *Adv. Chem. Phys.* **118** 99–190
- [3] Jamet M, Wernsdorfer W, Thirion C, Maily D, Dupuis V, Mélinon P and Pérez A 2001 Magnetic anisotropy of a single cobalt nanocluster *Phys. Rev. Lett.* **86** 4676–9
- [4] Wernsdorfer W 2009 From micro- to nano-SQUIDs: applications to nanomagnetism *Supercond. Sci. Technol.* **22** 064013
- [5] Hao L, Abmann C, Gallop J C, Cox D, Ruede F, Kazakova O, Josephs-Franks P, Drung D and Schurig T 2011 Detection of single magnetic nanobead with a nano-superconducting quantum interference device *Appl. Phys. Lett.* **98** 092504
- [6] Buchter A *et al* 2013 Reversal mechanism of an individual Ni nanotube simultaneously studied by torque and SQUID magnetometry *Phys. Rev. Lett.* **111** 067202
- [7] Schwarz T, Wölbing R, Reiche C F, Müller B, Martínez-Pérez M J, Mühl T, Büchner B, Kleiner R and Koelle D 2015 Low-noise YBa₂Cu₃O₇ nano-SQUIDs for performing magnetization-reversal measurements on magnetic nanoparticles *Phys. Rev. Appl.* **3** 044011
- [8] Martínez-Pérez M J, Müller B, Schwebius D, Korinski D, Kleiner R, Sesé J and Koelle D 2017 NanoSQUID magnetometry of individual cobalt nanoparticles grown by focused electron beam induced deposition *Supercond. Sci. Technol.* **30** 024003
- [9] Martínez-Pérez M J, Pablo-Navarro J, Müller B, Kleiner R, Magén C, Koelle D, de Teresa J M and Sesé J 2018 NanoSQUID magnetometry on individual as-grown and annealed Co nanowires at variable temperature *Nano Lett.* **18** 7674–82
- [10] Martínez-Pérez M J, Müller B, Lin J, Rodriguez L A, Snoeck E, Kleiner R, Sesé J and Koelle D 2020 Magnetic vortex nucleation and annihilation in bi-stable ultrasmall ferromagnetic particles *Nanoscale* **12** 2587–95
- [11] Bouchiat V 2009 Detection of magnetic moments using a nano-SQUID: limits of resolution and sensitivity in near-field SQUID magnetometry *Supercond. Sci. Technol.* **22** 064002
- [12] Nagel J *et al* 2011 Resistively shunted YBa₂Cu₃O₇ grain boundary junctions and low-noise SQUIDs patterned by a focused ion beam down to 80 nm linewidth *Supercond. Sci. Technol.* **24** 015015
- [13] Wölbing R, Schwarz T, Müller B, Nagel J, Kemmler M, Kleiner R and Koelle D 2014 Optimizing the spin sensitivity of grain boundary junction nanoSQUIDs—towards detection of small spin systems with single-spin resolution *Supercond. Sci. Technol.* **27** 125007
- [14] Granata C and Vettoliere A 2016 Nano superconducting quantum interference devices: a powerful tool for nanoscale investigations *Phys. Rep.* **614** 1–69
- [15] Martínez-Pérez M J and Koelle D 2017 NanoSQUIDs: basics & recent advances *Phys. Sci. Rev.* **2** 20175001
- [16] Kirtley J R, Ketchen M B, Stawiasz K G, Sun J Z, Gallagher W J, Blanton S H and Wind S J 1995 High-resolution scanning SQUID microscope *Appl. Phys. Lett.* **66** 1138–40
- [17] Kirtley J R 2009 Prospects for imaging magnetic nanoparticles using a scanning SQUID microscope *Supercond. Sci. Technol.* **22** 064008
- [18] Hazra D, Kirtley J R and Hasselbach K 2013 Nano-superconducting quantum interference devices with continuous read out at millikelvin temperatures *Appl. Phys. Lett.* **103** 093109
- [19] Kirtley J R *et al* 2016 Scanning SQUID susceptometers with sub-micron spatial resolution *Rev. Sci. Instrum.* **87** 093702
- [20] Reith P, Wang X R and Hilgenkamp H 2017 Analysing magnetism using scanning SQUID microscopy *Rev. Sci. Instrum.* **88** 123706
- [21] Wyss M, Gliga S, Vasyukov D, Ceccarelli L, Romagnoli G, Cui J, Kleibert A, Stamps R L and Poggio M 2019 Stray-field imaging of a chiral artificial spin ice during magnetization reversal *ACS Nano* **13** 13910–6

- [22] Anahory Y *et al* 2020 SQUID-on-tip with single-electron spin sensitivity for high-field and ultra-low temperature nanomagnetic imaging *Nanoscale* **12** 3174–82
- [23] Uri A *et al* 2020 Nanoscale imaging of equilibrium quantum Hall edge currents and of the magnetic monopole response in graphene *Nat. Phys.* **16** 164–70
- [24] Wyss M, Bagani K, Jetter D, Marchiori E, Vervelaki A, Gross B, Ridderbos J, Gliga S, Schönenberger C and Poggio M 2022 Magnetic, thermal, and topographic imaging with a nanometer-scale SQUID-on-cantilever scanning probe *Phys. Rev. Appl.* **17** 034002
- [25] Persky E, Sochnikov I and Kalisky B 2022 Studying quantum materials with scanning SQUID microscopy *Annu. Rev. Condens. Matter Phys.* **13** 385–405
- [26] Schwarz T, Nagel J, Wölbing R, Kemmler M, Kleiner R and Koelle D 2013 Low-noise nano superconducting quantum interference device operating in tesla magnetic fields *ACS Nano* **7** 844–50
- [27] Wölbing R, Nagel J, Schwarz T, Kieler O, Weimann T, Kohlmann J, Zorin A B, Kemmler M, Kleiner R and Koelle D 2013 Nb nano superconducting quantum interference devices with high spin sensitivity for operation in magnetic fields up to 0.5 T *Appl. Phys. Lett.* **102** 192601
- [28] Meltzer A Y, Uri A and Zeldov E 2016 Multi-terminal multi-junction dc SQUID for nanoscale magnetometry *Supercond. Sci. Technol.* **29** 114001
- [29] Uri A *et al* 2016 Electrically tunable multi-terminal SQUID-on-tip *Nano Lett.* **16** 6910–5
- [30] Drung D and Mück M 2004 SQUID electronics *The SQUID Handbook: Fundamentals and Technology of SQUIDs and SQUID Systems* ed J Clarke and A I Braginski vol I (Weinheim: Wiley-VCH) ch 4
- [31] Stewart W C 1968 Current-voltage characteristics of Josephson junctions *Appl. Phys. Lett.* **12** 277–80
- [32] McCumber D E 1968 Effect of ac impedance on dc voltage-current characteristics of Josephson junctions *J. Appl. Phys.* **39** 3113–8
- [33] Chesca B, Kleiner R and Koelle D 2004 SQUID theory *The SQUID Handbook: Fundamentals and Technology of SQUIDs and SQUID Systems* ed J Clarke and A I Braginski vol I (Weinheim: Wiley-VCH) ch 2
- [34] de Waal V J, Schrijner P and Llorca R 1984 Simulation and optimization of a dc SQUID with finite capacitance *J. Low Temp. Phys.* **54** 215–32
- [35] Hagedorn D, Kieler O, Dolata R, Behr R, Müller F, Kohlmann J and Niemeyer J 2006 Modified fabrication of planar sub- μm superconductor–normal metal–superconductor Josephson junctions for use in a Josephson arbitrary waveform synthesizer *Supercond. Sci. Technol.* **19** 294–8
- [36] Kieler O F, Iuzzolino R and Kohlmann J 2009 Sub- μm SNS Josephson junction arrays for the Josephson arbitrary waveform synthesizer *IEEE Trans. Appl. Supercond.* **19** 230–3
- [37] Bechstein S, Köhn C, Drung D, Storm J-H, Kieler O, Morosh V and Schurig T 2017 Investigation of nanoSQUID designs for practical applications *Supercond. Sci. Technol.* **30** 034007
- [38] Morosh V *et al* 2020 Transport and noise properties of sub-100-nm planar Nb Josephson junctions with metallic HfTi barrier for nanoSQUID applications *Phys. Rev. Appl.* **14** 054072
- [39] Nagel J, Kieler O F, Weimann T, Wölbing R, Kohlmann J, Zorin A B, Kleiner R, Koelle D and Kemmler M 2011 Superconducting quantum interference devices with submicron Nb/HfTi/Nb junctions for investigation of small magnetic particles *Appl. Phys. Lett.* **99** 032506
- [40] Martínez-Pérez M J, Gella D, Müller B, Morosh V, Wölbing R, Sesé J, Kieler O, Kleiner R and Koelle D 2016 Three-axis vector nano superconducting quantum interference device *ACS Nano* **10** 8308–15
- [41] Wolter S, Linek J, Altmann J, Weimann T, Bechstein S, Kleiner R, Beyer J, Koelle D and Kieler O 2021 Fabrication process for deep sub-micron SQUID circuits with three independent niobium layers *Micromachines* **12** 350
- [42] Khapaev M M, Kupriyanov M Y, Goldobin E and Siegel M 2003 Current distribution simulation for superconducting multi-layered structures *Supercond. Sci. Technol.* **16** 24–27